Journal of Alloys and Compounds 509 (2011) 6117–6122

Contents lists available at ScienceDirect

Journal of Alloys and Compounds

journal homepage: www.elsevier.com/locate/jallcom

Structural stability, electronic and optical properties of Ni-doped 3C–SiC by first principles calculation

Yankun Dou[a], Hai-bo Jin[a,*], Maosheng Cao[a], Xiaoyong Fang[b], Zhiling Hou[c], Dan Li[a], S. Agathopoulos[d]

[a] School of Materials Science and Engineering, Beijing Institute of Technology, Beijing 100081, PR China
[b] School of Science, Yanshan University, Qinhuangdao 066004, PR China
[c] School of Science, Beijing University of Chemical Technology, Beijing 100029, PR China
[d] Department of Materials Science and Engineering, University of Ioannina, GR – 451 10 Ioannina, Greece

ARTICLE INFO

Article history:
Received 14 November 2010
Received in revised form 6 March 2011
Accepted 8 March 2011
Available online 16 March 2011

Keywords:
Ni-doped 3C–SiC
First principle
Electronic property
Optical property

ABSTRACT

Structural stability along with the electronic and the optical properties of intrinsic 3C–SiC and Ni-doped 3C–SiC were studied by the first principles calculation. For the Ni-doped 3C–SiC, substitution of Ni in Si sub-lattice is energetically more favorable than that in C sub-lattice. Some new impurity energy levels appear in the band gap of Ni-doped 3C–SiC, which can improve the conductivity of 3C–SiC. The imaginary part of the dielectric function of Ni-doped 3C–SiC has three remarkable peaks at 0.69 eV, 2.35 eV, and 4.16 eV. This reveals that doping with Ni can improve the photo-absorption efficiency of 3C–SiC. In the absorption spectrum of Ni-doped 3C–SiC, the absorption edge red-shifts towards the far-infrared region. Furthermore, three new absorbing peaks emerge in the near-infrared region, visible region, and middle-ultraviolet region. These features confer Ni-doped 3C–SiC qualifications of a promising optical material.

1. Introduction

Silicon carbide is an attractive material because it is used in a wide variety of applications, due to excellent strength and chemical resistance and stability at high temperatures, semi-conductivity features, high thermal stability, and thermal conductivity [1–3].

Nevertheless, 3C–SiC is a wide band gap semiconductor with an absorption edge in the ultraviolet region as well as a poor absorber of photons in the solar spectrum. The n- or p-type doping of 3C–SiC is a promising way to modify the host properties of 3C–SiC in many applications [4,5]. It has been shown that doping of P in 3C–SiC makes the photoluminescence (PL) lines broader and the conductivity better as compared to the intrinsic 3C–SiC, P-doped 4H-, and 6H–SiC [6]. The complex permittivity of SiC powders decreases first and then increases with increasing B content [7]. The dielectric dissipation factor of N-doped 3C–SiC particles is higher than that of pure 3C–SiC particles [8]. Neutral impurity scattering can be the main mechanism for interpreting the low frequency conductivity of N-doped 3C–SiC [9]. Better results of microwave dielectric loss were achieved in the X-band of p-type doped 3C–SiC (than in pure 3C–SiC) [10–12].

The 3d-transition metals have recently been considered as efficient dopants for altering and controlling the electrical and magnetic properties of 3C–SiC [13]. The magnetism of Mn-doped 3C–SiC can be enhanced via growing a structure with Mn in Si sites, which can result in localized magnetic interactions [14]. Moreover, Mn-doped 3C–SiC has semi-metallic properties with a fast mobility of conduction electrons [15]. V-doped 3C–SiC nano-wires can exhibit semi-metallic ferromagnetic properties and reduce magnetic semiconductor behavior at very low temperatures [16].

The electrical and magnetic properties of 3C–SiC doped with 3d-metals have recently been studied by the method of linear muffin-tin orbitals (LMTOs) using the tight-binding approximation and the super-cell model [1,17–20]. It has been revealed that most of the 3d-dopants mainly occupy the Si sub-lattice sites in 3C–SiC, but Mn is expected to occupy the C sub-lattice sites [17]. The Cr- or Mn-doped 3C–SiC has magnetic moment, but the Ni-, Fe-, and Co-doped 3C–SiC does not exhibit any magnetic moment [20]. Furthermore, Ni-doped 3C–SiC features semi-metallic properties and rather weak relaxation effects [1].

A literature survey reveals that there are only few theoretical, based on density functional theory (DFT), and experimental studies on Ni-doped 3C–SiC. Therefore, the structural, electronic, and optical properties of Ni-doped 3C–SiC were studied in this paper using the first-principle calculation, to evaluate the potential of this material in modern technological applications.

2. Models and calculations

SiC exhibits more than 200 poly-types with different stacking sequences of essentially identical Si–C bilayers [21], such as 3C–SiC, 2H–SiC, 4H–SiC, and 6H–SiC. In the present study, the adopted SiC

* Corresponding author. Tel.: +86 10 68914062; fax: +86 10 68914062.
E-mail address: hbjin@bit.edu.cn (H.-b. Jin).

0925-8388/$ – see front matter © 2011 Elsevier B.V. All rights reserved.
doi:10.1016/j.jallcom.2011.03.058

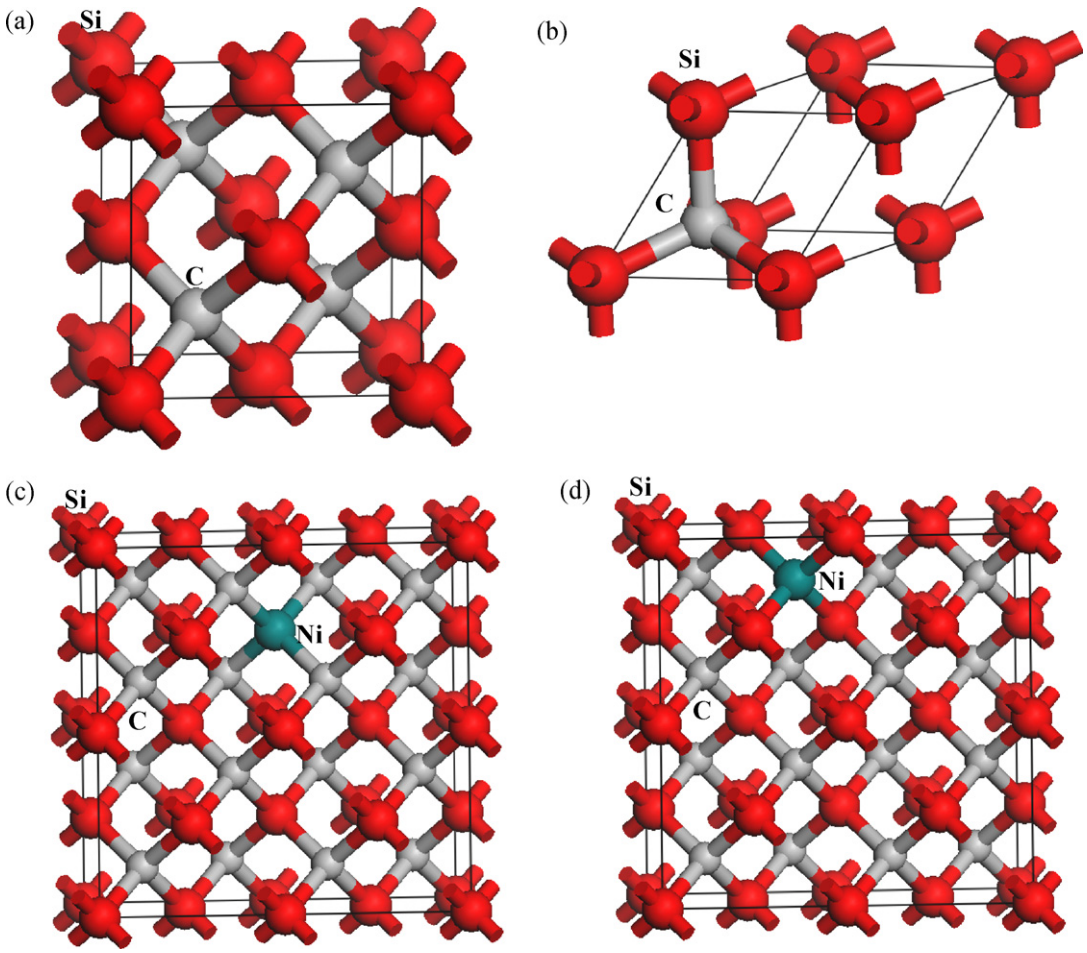

Fig. 1. (a) 3C–SiC crystal structure, (b) a primitive cell of 3C–SiC, (c) $Si_{15}Ni_1C_{16}$ crystal structure, and (d) $Si_{16}Ni_1C_{15}$ crystal structure.

model is cubic SiC with zinc blend structure (labeled as 3C–SiC) and space group of *F*-43*m*. The structure of 3C–SiC is shown in Fig. 1a, with equilibrium lattice parameters of $a = b = c = 4.348$ Å, and $\alpha = \beta = \gamma = 90^\circ$. The 3C–SiC crystal structure, shown in Fig. 1a, comprises two face-centered cubic unit cells, and the Si unit cell is nested in the C unit cell. Each atom connects with the nearest-neighboring four adjacent atoms of other species by covalent bonds. A primitive cell of 3C–SiC is shown in Fig. 1b. A standard-size super-cell with 32 atoms was built from the conventional 8-atoms cubic unit cell of 3C–SiC with a $2 \times 2 \times 1$ replication. The structure of Ni-doped 3C–SiC was then modeled by introducing a Ni atom to replace a Si atom (Fig. 1c) or a C atom (Fig. 1d), corresponding to Ni concentration of c.a. 3.125 mol%.

The calculations were carried out using first-principles plane-wave pseudo-potential with Cambridge Serial Total Energy Package (CASTEP) code, which is based on density functional theory and molecular dynamics theory [22]. The calculations were performed using the generalized gradient approximation (GGA) method and the exchange-correlation function was realized by Perdew–Burke–Emzerhof (PBE) [23]. Ni-doped 3C–SiC is a strongly correlated system, which requires another approach to take into account the Coulomb interactions among d electrons. It has been proven that the density functional theory (DFT) + U approach [24,25] is an effective tool to study the strongly correlated systems. Ouyang et al. [26] studied the electronic structure of $LiMn_2O_4$ with the DFT + U method and the results agreed fairly well with the experimental findings. In our study, the calculations were performed with LDA + U, allowing U to vary from 0 to 5.5 eV. By comparing the results with different U values, a good value of U = 4.5 eV was obtained for an accurate calculation. The valence electron configurations of Ni-doped 3C–SiC are Si: $3s^2 3p^2$, C: $2s^2 2p^2$, and Ni: $3d^8 4s^2$. The integrations over the Brillouin zone were replaced by discrete summation over a special set of *k* points using the Monkhorst–Pack scheme [27]. The plane-wave cut-off energy of 330 eV and a $2 \times 2 \times 3$ grid of Monkhorst–Pack points for $2 \times 2 \times 1$ super-cell have been employed in this study to ensure good convergence of the computed structures and energies.

In the self-consistent field computations, the ground state energy was calculated using the Pulay density mixed method, and the self-consistent field was set to 5×10^{-7} eV atom^{-1}. The structure, the cell parameters, and the atomic positions of the doped system were optimized with the Broyden and Goldfarb (BFGS) method [28]. The stability of the system is better as long as the four optimization parameters, calculated at the same time, all meet the convergence standard. The four optimization parameters are as follows: (1) the convergence standard of interaction between electrons is 0.01 eV/Å, (2) the convergence standard of the individual-atom energy is 5×10^{-6} eV atom^{-1}, (3) the convergence standard of crystal internal stress is 0.02 GPa, and (4) the convergence standard for maximum shift of atom is 5×10^{-4} Å.

3. Results and discussion

3.1. Structural stability of Ni-doped 3C–SiC

The preferential substituting position of Ni in 3C–SiC super-cell can be determined by calculating the formation energy E_f either at Si site or C site. In our calculations, the formation energy of a

charged point defect in SiC, E_f^q, can be expressed as [29,30]

$$E_f^q = E(n_{Si}, n_C, n_{Ni}, q) - n_{Si}\mu_{Si} - n_C\mu_C - n_{Ni}\mu_{Ni} - qE_F \quad (1)$$

where $E(n_{Si},nc,n_{Ni},q)$ is the total super-cell energy, and n_{Si}, n_C, and n_{Ni} represent the number of moles of Si, C, and Ni-doped atoms, respectively. The chemical potential of Si, C, and Ni are μ_{si}, μ_C, and μ_{Ni}, respectively, and q is the charge state of the defect. E_F is the Fermi level, which is located between the top of the valence band (E_v) and the bottom of the conduction band (E_c). The chemical potentials of Si and C atoms in the thermal equilibrium regime of SiC must satisfy the thermodynamic stability condition

$$\mu_{Si} + \mu_C = \mu_{SiC(bulk)} \quad (2)$$

where $\mu_{SiC(bulk)}$ is the chemical potential of SiC in the zinc-blende structure. The allowed ranges of μ_{Si} and μ_C are determined by the heat enthalpy, ΔH_f^{SiC}, defined as

$$\Delta H_f^{SiC} = \mu_{SiC(bulk)} - \mu_{Si(bulk)} - \mu_{C(bulk)} \quad (3)$$

where $\mu_{Si(bulk)}$ and $\mu_{C(bulk)}$ are the chemical potentials of Si and C respectively in the diamond structure, and they follow Eq. (4) [31]

$$\Delta\mu = \mu_{Si} - \mu_{Si(bulk)} - 0.5\Delta H_f^{SiC} = 0.5\Delta H_f^{SiC} - \mu_C + \mu_{C(bulk)} \quad (4)$$

Theoretically, the tuning of C/Si ratio during growth is limited by the condition of $\mu_{Si} = \mu_{Si(bulk)}$ in a Si-rich regime, and $\mu_C = \mu_{C(bulk)}$ in a C-rich regime. Thus, Eq. (3) requires

$$0.5\Delta H_f^{SiC} \le \Delta\mu \le -0.5\Delta H_f^{SiC} \quad (5)$$

Our calculated value of heat enthalpy ΔH_f^{SiC} is −0.644 eV/SiC, which agrees fairly well with the experimental value of −0.68 eV/SiC [32].

The values of E_f for Ni impurity at Si and C sites are 4.074 eV and 4.793 eV, respectively. All relevant parameters are presented in Table 1. Accordingly, it is concluded that E_f for Ni-impurity at the Si site is lower than that at the C site, which indicates that the substitutional Ni is more stable in the Si sub-lattice than that in the C sub-lattice. Therefore, we shall focus our investigation only on the properties of Ni accommodated in the Si sub-lattice in 3C–SiC.

3.2. Energy band structures and density of states (DOS)

In Fig. 2, the calculated band structures of intrinsic 3C–SiC and Ni-doped 3C–SiC are presented. The band structure of Ni-doped 3C–SiC becomes more complicated as compared to the intrinsic 3C–SiC, since there is a significant difference of energy levels and band gaps for the intrinsic 3C–SiC and the Ni-doped 3C–SiC.

From Fig. 2a, it can be seen that the top of the valence band (VB) of intrinsic 3C–SiC is in the Brillouin center (G-point) with three-fold degeneration, and the bottom of the conduction band (CB) is located at the Brillouin boundary X-point with two-fold degeneration. This is a typical characteristic of indirect band gap for a zinc-blende structure. The band gap of intrinsic 3C–SiC is 1.501 eV, calculated with CASTEP, which is close to the experimental value of 2.42 eV [33]. Moreover, Santos et al. have calculated by first principles that the value of the band gap of 3C–SiC is 1.32 eV, which is lower than that yielded from our calculations [34]. The theoretical value is smaller than the experimental value because the correlation interaction between excited electrons in the calculation model has been underestimated, according to the Ref. [35].

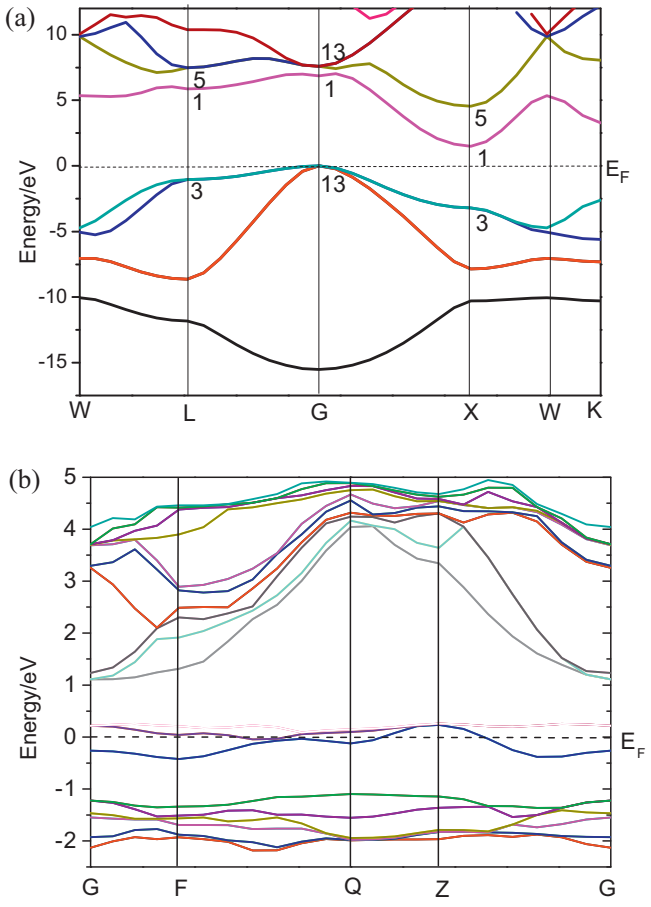

Fig. 2. The band structures of (a) intrinsic 3C–SiC and (b) Ni-doped 3C–SiC.

According to Fig. 2b, the band structure of Ni-doped 3C–SiC has more energy levels. The bottom of CB is at the G-point, and the top of the VB is at the Q-point, which show that Ni-doped 3C–SiC is also an indirect band structure. Due to the doping of Ni in 3C–SiC structure, there are some non-filled impurity energy levels in the neighborhood of Fermi level, and these impurity energy levels mainly originate from the 3d orbital electrons of Ni. The emergence of these energy levels would lead to the electronic intra-band or inter-band transition from the occupied bands to the unoccupied ones under irradiation. This may induce intense absorption in the long wavelength visible region [36]. From Fig. 2b, it seems that a part of the 3d energy levels below E_F has a large curvature between F- and Q-points, suggesting a small effective mass for hole transport [37]. It is expected that the excited holes in the Ni-doped 3C–SiC move freely and quickly, which may promote the electrons in the VB to jump to the impurity energy levels. In other words, this means that the transition probability increases to some extent. The electron

Table 1
Formation energy E_f and total super-cell energy $E(n_{Si},nc,n_{Ni},q)$ of 3C–SiC with Ni substituting Si or C atoms, chemical potentials of bulk Si ($\mu_{Si(bulk)}$) and C ($\mu_{C(bulk)}$) in diamond structure, chemical potential of SiC $\mu_{SiC(bulk)}$ in zinc-blende structure, heat enthalpy ΔH_f^{SiC}, and chemical potentials of Ni (μ_{Ni}), Si (μ_{Si}), and C (μ_C) (units in eV).

Magnitude	Replaced site		
	Si		C
$E(n_{Si},n_C,n_{Ni},q)$	−5449.203		−5400.868
$\mu_{Si(bulk)}$		−107.325	
$\mu_{C(bulk)}$		−154.941	
$\mu_{SiC(bulk)}$		−262.915	
ΔH_f^{SiC}		−0.644	
μ_{Ni}		−1354.356	
μ_{Si}		−107.647	
μ_C		−155.263	
E_f	4.074		4.793

conductivity, σ, is

$$\sigma = \frac{pe^2\tau_p}{m_p^*} \tag{6}$$

where p is the hole density, τ_p is the carrier lifetime, and m_p^* is the effective mass of a hole. The impurity energy levels lead to a high hole-density and a small effective mass. Accordingly, electron conductivity of Ni-doped 3C–SiC is improved.

The total DOS and partial density of states (PDOS) for intrinsic 3C–SiC and Ni-doped 3C–SiC are shown in Fig. 3. According to Fig. 3a, the electron spectrum of the DOS contains two bands, i.e. the VB and the CB. The low-energy VB is from −16 eV to −9 eV, which mainly originates from the 2s orbital electrons in C. The upper occupied VB is from −8 eV to 0 eV, which is mainly composed of 2p orbital electrons in C. Meanwhile, the 3p and 3s orbital electrons of Si also contribute to the upper occupied VB. The CB mainly consists of 3p orbital electrons of Si and a few 2p orbital electrons of C.

The effect of the 3d orbital electrons on DOS for Ni-doped 3C–SiC is shown in Fig. 3b. It can be seen that whole DOS moves towards low energy and E_F also moves towards the CB. There is an additional intense peak arising around E_F, due to hybridization of Ni 3d, Si 3p, and C 2p states. The intense peak near E_F favors electron transition, which increases the conductivity of Ni-doped 3C–SiC. It is evident that introduction of Ni leads to a semi-metal nature of 3C–SiC, which agrees with the calculated results of the band structure. The low-energy VB is also controlled by the 2s orbital electrons in C, and the upper occupied VB originates from Si 3s, C 2p, and Ni 3d electrons. The CB is mainly composed of Si 3p electrons. The top of the new emerging peak of the total DOS is located at the right of

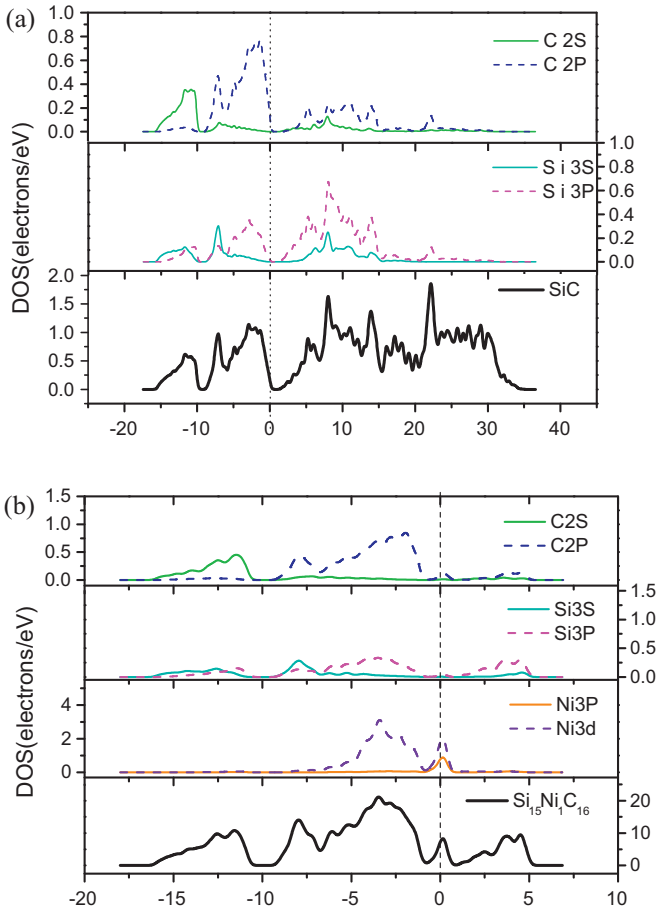

Fig. 3. Total and partial density of states for (a) intrinsic 3C–SiC and (b) Ni-doped 3C–SiC.

E_F, implying that 3d impurity energy levels are not fulfilled by electrons; thus, hole conduction effect is expected for Ni-doped 3C–SiC [1].

3.3. Optical properties

The optical properties of intrinsic 3C–SiC and Ni-doped 3C–SiC were investigated on the basis of electronic structure calculations. The imaginary part $\varepsilon_2(\omega)$ and the real part $\varepsilon_1(\omega)$ of the dielectric function, which accounts for the photo-absorption property, are shown in Fig. 4. The real part and the imaginary part of the dielectric function of the Ni-doped 3C–SiC are very different from those ones of intrinsic 3C–SiC. The imaginary and the real parts of the dielectric function of intrinsic 3C–SiC are rather flat below 5.1 eV. There are many critical points appearing in the calculated imaginary part of dielectric function from 5.1 eV to 10 eV, which is similar to the results of the pseudo-potential (PP) approach, obtained by Theodorou et al. [38]. The imaginary part $\varepsilon_2(\omega)$ of the dielectric function is directly connected with the energy band structure (Fig. 2a). Hence, the absorption starting from ~5.1 eV is related to the X3-to-X1 transition. There are five critical points between 5.1 eV and 10 eV, *i.e.* 5.83 eV, 7.23 eV, 8.42 eV, 8.80 eV, and 9.35 eV. The first three points are mainly related to the transitions of G13-G1, L3-L1, and G13-G13. The last two critical points result from the transitions of X3-X5 and L3-L5. These main points are consistent with the experimental results measured with ultraviolet spectroscopic ellipsometry, which are located at 5.92 eV, 7.41 eV, 8.44 eV, 8.97 eV, and 9.35 eV [39]. Moreover, the imaginary part of the dielectric function for Ni-doped 3C–SiC appears at a lower absorption edge, compared to intrinsic 3C–SiC. As shown in Fig. 4, three obvious peaks emerge at 0.69 eV, 2.35 eV, and 4.16 eV, which are located in the middle-infrared region, visible region, and middle-ultraviolet region, respectively.

The imaginary part of the dielectric function is

$$\varepsilon_2 = \frac{\omega\sigma}{\varepsilon_0[\tau_p^2\left(\omega_0^2 - \omega^2\right)^2 + \omega^2]} \tag{7}$$

where ω denotes the frequency of the light, ω_0 is the average frequency of long-wavelengths of optical wave in the crystal lattice, and ε_0 is the dielectric constant in vacuum. The increase of σ can lead to the improvement of $\varepsilon_2(\omega)$, which explains the high intensity of the new peaks of $\varepsilon_2(\omega)$. The locations of the new peaks are determined by

$$\hbar\omega_0 = E_i - E_j \tag{8}$$

where $\hbar$ is the Planck's constant, and E_i and E_j are the original energy of transition electrons and the energy of electrons after transition, respectively. A molecular-orbital bonding schematic representation to describe the orbitals of Ni-doped 3C–SiC is shown in Fig. 4b. For both 3C–SiC and Ni-doped 3C–SiC, the large gap between the bands *a* and *d* mainly originates from the bonding C-2p orbitals and the anti-bonding Si-3p orbitals. Doping with Ni in 3C–SiC results in the generation of the bands *c* and *b* in the band gap of 3C–SiC. According to Eq. (8), the first sharp peak at 0.69 eV primarily results from the excitations from band *c* to band *b*. The peaks at 2.35 eV and 4.16 eV, which increase the absorption, may result from transitions from the VB (band *d*) to band *b* just above E_F, but may also result from transitions from band *c* to the CB (band *a*). The reason for the sharp increase of absorption from about 5.1 eV is mainly attributed to the excitations from the VB to the CB. The absorption starts from 0.05 eV. Thus, the absorption edge of Ni-doped 3C–SiC shifts towards the far-infrared region, which can improve the photo-absorption efficiency.

The absorption function can be calculated from the imaginary part and the real part of the dielectric function. Meanwhile, the scis-

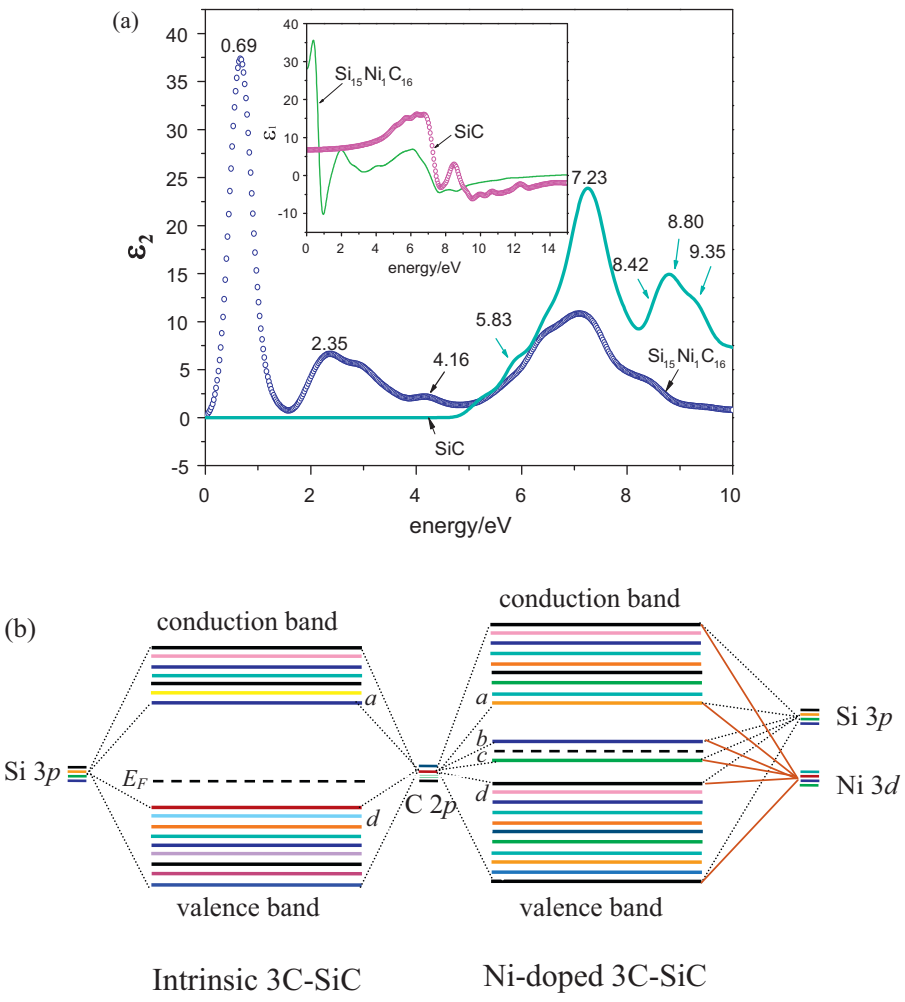

Fig. 4. (a) Imaginary part and real part of the dielectric function of intrinsic 3C–SiC and Ni-doped 3C–SiC. (b) Molecular-orbital bonding structures for intrinsic 3C–SiC and Ni-doped 3C–SiC.

sors method can be used to make the calculated results closer to the experimental data [40]. The relationship between the absorption coefficient $\alpha(\omega)$ and the imaginary part of the dielectric function $\varepsilon_2(\omega)$ is given by Eq. (9)

$$\alpha = \frac{\omega\varepsilon_2}{cn} \tag{9}$$

where n is the real part of refraction index and c is the speed of light in vacuum. Apparently, $\alpha(\omega)$ is directly proportional to $\varepsilon_2(\omega)$.

The calculated spectra $\alpha(\omega)$ of intrinsic and Ni-doped 3C–SiC by first principles are shown in Fig. 5. In the absorption spectrum of intrinsic 3C–SiC, there is no-peak at low frequency but only three major absorption peaks at 7.5 eV, 9.6 eV, and 12.7 eV. These peaks mainly originate from the excitations of C-2p electrons. It is interesting that there are three new peaks emerging at 0.92 eV, 3.11 eV, and 4.21 eV in the absorption spectrum of Ni-doped 3C–SiC. These three peaks, shown in the inset of Fig. 5, correspond to the new peaks in the imaginary part $\varepsilon_2(\omega)$ of the dielectric function and coincide with the results obtained from Eq. (9).

These new emerging peaks suggest an increase of transition probability of excited electrons, which is consistent with the analysis of the Ni-doped 3C–SiC band structure. The peaks above 5.0 eV are similar to those of intrinsic 3C–SiC. The peak at 0.92 eV in the infrared region is due to the transitions of electrons between the Ni 3d orbitals. The two peaks at 3.0 eV and 4.2 eV may originate from the transitions of C-2p electrons at the top of VB, into Ni-3d above the Femi energy, or the Ni-3d electrons below the Femi

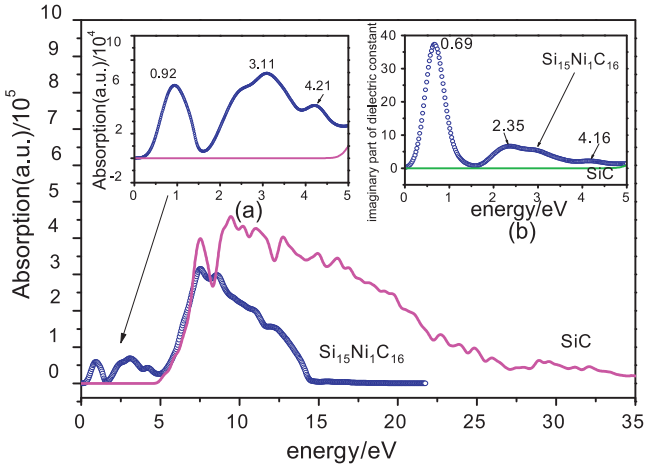

Fig. 5. The absorption spectra of intrinsic 3C–SiC and Ni-doped 3C–SiC. Inset (a): Low-frequency absorption spectra. Inset (b): Imaginary part of low-frequency dielectric function.

energy into the Si-3p at the bottom of CB. These two peaks appear in the visible region and the middle-ultraviolet region, respectively. The three remaining peaks at about 7.5 eV, 8.6 eV, and 12.0 eV in the absorption spectrum of Ni-doped 3C–SiC result from the transitions of C-2p orbital electrons from the VB to the bottom of CB.

As shown in Fig. 5, the absorption edge red-shifts towards the far-infrared region. This apparently occurs because of the increase the free carrier density due to doping with Ni.

4. Conclusions

The calculated formation energy reveals that Ni-doped 3C–SiC is more stable for Ni accommodated in the Si sub-lattice than in the C sub-lattice. The intrinsic 3C–SiC is an indirect band gap (1.501 eV) semiconductor. For the Ni-doped 3C–SiC, new impurity energy levels emerge in the band gap, which favors the transition of electrons. In Ni-doped 3C–SiC, three new peaks appear in the imaginary part of the dielectric function at 0.69 eV, 2.35 eV, and 4.16 eV, which suggests that the doping of 3C–SiC with Ni can improve the photo-absorption efficiency and the conductivity of 3C–SiC. Moreover, the absorption edge of the absorption spectrum for Ni-doped 3C–SiC red-shifts towards the far-infrared region and three new peaks emerge at 0.92 eV, 3.11 eV, and 4.21 eV. These features qualify Ni-doped 3C–SiC for further consideration as potential material for optical applications.

Acknowledgements

The authors gratefully acknowledge the financial support of the National Natural Science Foundation of P.R. China under the Grants 50672010 and 50972015.

References

[1] N.I. Medvedeva, É.I. Yuryeva, A.L. Ivanovskiĭ, Semiconductors 36 (2002) 751–754.
[2] X.M. Yu, W.C. Zhou, F. Luo, W.J. Zheng, D.M. Zhu, J. Alloys Compd. 479 (2009) L1–L3.
[3] J.S. Lee, Y.K. Byeun, S.H. Lee, S.C. Choi, J. Alloys Compd. 456 (2008) 257–263.
[4] G.Y. Feng, X.Y. Fang, J.J. Wang, Y. Zhou, R. Lu, J. Yuan, M.S. Cao, Physica B 405 (2010) 2625–2631.
[5] X.I. Su, W.C. Zhou, J. Xu, Z.M. Li, F. Luo, D.M. Zhu, J. Alloys Compd. 492 (2010) L16–L19.
[6] N.T. Son, A. Henry, J. Isoya, M. Katagiri, T. Umeda, Phys. Rev. B 73 (2006) 075201.
[7] Z.M. Li, W.C. Zhou, X.L. Su, F. Luo, Y.X. Huang, C. Wang, J. Alloys Compd. 509 (2011) 973–976.
[8] D.L. Zhao, F. Luo, W.C. Zhou, J. Alloys Compd. 490 (2010) 190–194.
[9] J.J. Wang, X.Y. Fang, G.Y. Feng, W.l. Song, Z.L. Hou, H.B. Jin, J. Yuan, M.S. Cao, Phys. Lett. A 374 (2010) 2286–2289.
[10] H.B. Jin, M.S. Cao, W. Zhou, S. Agathopoulos, Mater. Res. Bull. 45 (2010) 247–250.
[11] Z.M. Li, W.C. Zhou, T.M. Lei, F. Luo, Y.X. Huang, Q.X. Cao, J. Alloys Compd. 475 (2009) 506–509.
[12] Z.M. Li, W.C. Zhou, X.L. Su, Y.X. Huang, G.F. Li, Y.P. Wang, J. Am. Ceram. Soc. 92 (2009) 2116–2118.
[13] N. Theodoropoulou, A.F. Hebart, S.N.G. Chu, M.E. Overberg, C.R. Abernathy, S.J. Pearton, R.G. Wilson, J.M. Zavada, Electrochem. Solid-State Lett. 4 (2001) G119–G121.
[14] K. Bouziane, M. Mamor, M. Elzain, Phys. Rev. B 78 (2008) 195305.
[15] Y.S. Kim, Y.C. Chung, S.C. Yi, Mater. Sci. Eng. B 126 (2006) 194–196.
[16] H.K. Seong, T.E. Park, S.C. Lee, K.R. Lee, J.K. Park, H.J. Choi, Mater. Int. 15 (2009) 107–111.
[17] V.A. Gubanov, C. Boekema, Appl. Phys. Lett. 78 (2001) 216–218.
[18] É.I. Yurieva, J. Struct. Chem. 45 (2004) 194–200.
[19] K.O. Barbosa, W.V.M. Machado, L.V.C. Assali, Physica B 308 (2001) 726–729.
[20] N.I. Medvedeva, E.I. Yur'eva, A.L. Ivanovskiĭ, Semiconductors 37 (2003) 1243–1246.
[21] N.W. Jepps, T.F. Page, Prog. Cryst. Growth Charact. Mater. 7 (1983) 259–307.
[22] M.D. Segall, P. Lindan, M.J. Probet, C.J. Pickard, P.J. Hasnip, S.J. Clark, M.C. Payne, J. Phys. Condens. Matter 14 (2002) 2717–2744.
[23] J.P. Perdew, K. Burke, M. Ernzerhof, Phys. Rev. Lett. 77 (1996) 3865–3868.
[24] S.G. Park, B. Magyari-Köpe, Y. Nishi, Phys. Rev. B 82 (2010) 115109.
[25] A. Juhin, F. de Groot, G. Vankó, M. Calandra, C. Brouder, Phys. Rev. B 81 (2010) 1151115.
[26] C.Y. Ouyang, S.Q. Shi, M.S. Lei, J. Alloys Compd. 474 (2009) 370–374.
[27] H.J. Monkhorst, J.D. Pack, Phys. Rev. B 135 (1976) 5188–5192.
[28] T.H. Fische, J. Almlof, J. Phys. Chem. 96 (1992) 9768–9774.
[29] A. Zywietz, J. Furthmuller, F. Bechstedt, Phys. Rev. B 59 (1999) 15166–15180.
[30] C.G. Vandewalle, Phys. Rev. B 49 (1994) 4579–4585.
[31] B. Aradi, A. Gali, P. Deák, J.E. Lowther, N.T. Son, E. Janzén, W.J. Choyke, Phys. Rev. B 63 (2001) 245202.
[32] O. Madelung, M. Schulz, H. Weiss, Numerical Data and Functional Relationships in Science and Technology, second ed, Springer, New York, 1982.
[33] R.G. Humphreys, D. Bimberg, W.J. Choyke, Sold State Commun. 39 (1981) 163–167.
[34] I.S. Santos, D.E. Oliveira, R.H. Miwa, Phys. Rev. B 79 (2009) 085427.
[35] J.P. Perdew, A. Zunger, Phys. Rev. B 23 (1981) 5048–5079.
[36] X.H. Yu, C.S. Li, Y. Ling, T.A. Tang, Q. Wu, J.J. Kong, J. Alloys Compd. 507 (2010) 33–37.
[37] X.G. Xu, X. Ding, Q. Chen, L.M. Peng, Phys. Rev. B 73 (2006) 165403.
[38] G. Theodorou, G. Tsegas, E. Kaxiras, J. Appl. Phys. 85 (1999) 2179–2184.
[39] J. Petalas, S. Logothetidis, M. Gioti, C. Janowitz, Phys. Status Solidi B 209 (1998) 499–521.
[40] J.B. Li, S.H. Wei, S.S. Li, J.B. Xia, Phys. Rev. B 74 (2006) 081201.